www.elsevier.com/locate/jmps

A micromechanical damage and fracture model for polymers based on fractional strain-gradient elasticity

S. Heyden, B. Li, K. Weinberg, S. Conti, M. Ortiz

PII: S0022-5096(14)00172-0
DOI: http://dx.doi.org/10.1016/j.jmps.2014.08.005
Reference: MPS2523

To appear in: *Journal of the Mechanics and Physics of Solids*

Received date: 11 January 2014
Revised date: 6 June 2014
Accepted date: 21 August 2014

Cite this article as: S. Heyden, B. Li, K. Weinberg, S. Conti and M. Ortiz, A micromechanical damage and fracture model for polymers based on fractional strain-gradient elasticity, *Journal of the Mechanics and Physics of Solids,* http://dx.doi.org/10.1016/j.jmps.2014.08.005

A micromechanical damage and fracture model for polymers based on fractional strain-gradient elasticity

S. Heyden[a], B. Li[a], K. Weinberg[b], S. Conti[c], M. Ortiz[a,*]

[a] *Division of Engineering and Applied Science, California Institute of Technology Pasadena, CA91125, USA*
[b] *Lehrstuhl für Festörpermechanik, Universität Siegen, D-57076 Siegen, Germany*
[c] *Institut für Angewandte Mathematik, Universität Bonn, Endenicher Allee 60, Bonn, 53115, Germany*

Abstract

We formulate a simple one-parameter macroscopic model of distributed damage and fracture of polymers that is amenable to a straightforward and efficient numerical implementation. We show that the macroscopic model can be rigorously derived, in the sense of *optimal scaling*, from a micromechanical model of chain elasticity and failure regularized by means of *fractional strain-gradient elasticity*. In particular, we derive optimal scaling laws that supply a link between the single parameter of the macroscopic model, namely, the critical energy-release rate of the material, and micromechanical parameters pertaining to the elasticity and strength of the polymer chains and to the strain-gradient elasticity regularization. We show how the critical energy-release rate of specific materials can be determined from test data. Finally, we demonstrate the scope and fidelity of the model by means of an example of application, namely, Taylor-impact experiments of polyurea 1000 rods.

Keywords:
Polymers, damage, failure, polyurea

1. Introduction

The use of polymers as structural materials is critically limited by their tendency to degrade by distributed damage or to fail by fracture, sometimes in a brittle manner (cf., e. g., Andrews (1968); Bikales (1971); Kinloch and Young (1983); Williams (1984); Kausch (1985); Grellmann and Seidler (2001); Argon (2013) for reviews). Damage in polymers deformed under tensile loading often takes the form of distributed voids (Jiao et al., 2006,

*Corresponding author
E-mail address: ortiz@aero.caltech.edu (M. Ortiz).

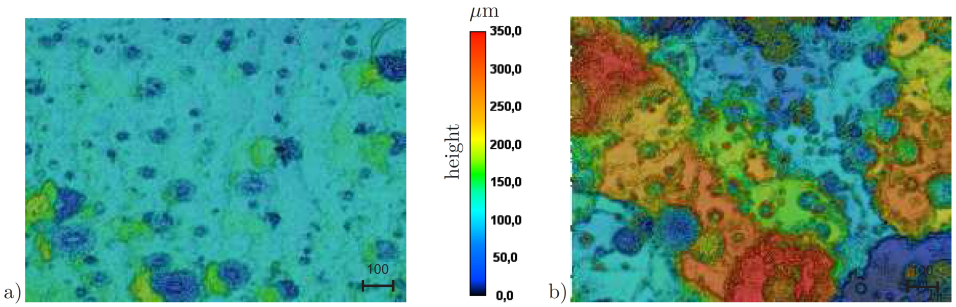

Figure 1: Surface profiles (height measured from the deepest point) of a polyurea specimen tested in uniaxial tension Weinberg and Reppel (2013). a) Initial profile showing initial porosity. b) Profile after fracture showing proliferation of voids.

2007, 2009; Weinberg and Reppel, 2013), cf. Fig. 1. Voids nucleate heterogeneously from flaws or inclusions, Fig. 1a, and subsequently grow under tension, Fig. 1b, resulting in softening—or loss of bearing capacity—of the material (cf., e. g., Gent (1973); Cho and Gent (1988); Gent and Wang (1991)). Likewise, fracture in polymers can often be traced to the formation of crazes (cf., e. g., Donald and Kramer (1982); Kausch (1983); Henkee and Kramer (1986); Kramer and Berger (1990); Sanderson and Pasch (2004)), Fig. 2. Crazes are thin layers of highly localized tensile deformation. The craze surfaces are bridged by numerous fine fibrils, themselves consisting of highly oriented chains, separated by connected voids. Crazes undergo several stages along their formation, including nucleation, growth and final breakdown, resulting in the formation of a traction-free crack, or fracture. Craze initiation is likely the result of heterogeneous cavitation at flaws loaded under conditions of high triaxiality. Craze propagation has been linked to a meniscus instability resulting in the formation of fibrils. This analogy is immediately suggestive of some role played by surface energy or other similar physical properties not accounted for by bulk behavior. Eventually, crazes break down to form cracks. Experimentally, crazes are easily identified and observed fractographically by a variety of techniques including optical interferometry, light reflectometry, dark-field electron microscopy, and others.

Owing to its engineering importance, polymer damage and fracture have been the focus of extensive modeling. A number of micromechanical and computational models, ranging from atomistic to continuum, have been put forth (cf., e. g., Leonov and Brown (1991); Krupenkin and Fredrickson (1999a,b); Tijssens et al. (2000a,b); Estevez et al. (2000a,b); Baljon and Robbins (2001); Socrate et al. (2001); Drozdov (2001); Tijssens and van der Giessen (2002); Rottler and Robbins (2003, 2004); Basu et al. (2005); Saad-Gouider et al. (2006); Zairi et al. (2008); Seelig and Van der Giessen (2009); Reina et al. (2013)), including consideration of nucleation and growth

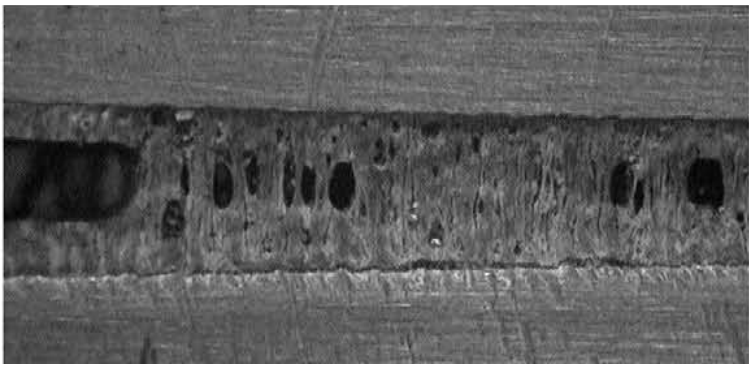

Figure 2: Crazing process in a steel/polyurea/steel sandwich specimen under opening mode fracture (Yong et al., 2009).

of voids, craze nucleation, network hardening and disentanglement, chain strength, surface energy and other, that account, to varying degrees, for the observational evidence and relate macroscopic properties to material structure and behavior at the microscale. In parallel a large mathematical literature has evolved, discussing the possibility of cavitation in local models and possible nonlocal extensions which may ensure existence of minimizers, see for example Ball (1982); James and Spector (1991); Müller and Spector (1995); Conti and DeLellis (2003); Henao and Mora-Corral (2010). These advances notwithstanding, the connection between micromechanical properties and polymer fracture, and specifically any scaling laws thereof, has defied rigorous analytical treatment and characterization. Of special interest is the identification of optimal scaling laws relating the macroscopic behavior to micromechanical and loading parameters. Such optimal scaling laws are established by producing upper and lower bounds of a power-law type with matching exponents for all parameters in both bounds. Optimal scaling methods were pioneered by Kohn and Müller (1992) as part of their seminal work on branched structures in martensite, and have been since successfully applied to a number of related problems, including shape-memory alloys, micromagnetics, crystal plasticity, and others (Kohn and Müller, 1992, 1994; Choksi et al., 1999; Conti, 2000; Conti and Ortiz, 2005).

Fokoua et al. (2013, 2014) have recently applied those analysis tools to ductile fracture of metals. They specifically consider the deformation, ultimately leading to fracture, of a slab of finite thickness subject to monotonically-increasing normal opening displacements on its surfaces. In addition, they posit two competing constitutive properties, namely, sublinear energy growth and strain-gradient hardening. Sublinear growth (the energy of linear elasticity exhibits quadratic growth, by way of comparison) is a reflection of the work-hardening characteristics of conventional metallic specimens and gives rise to well-known geometric instabilities such as the necking of bars, sheet

necking, strain localization and others (cf., e. g., McClintock and Argon (1966)). In metals undergoing ductile fracture this inherently unstable behavior is held in check by a second fundamental property of metals, namely, *strain-gradient hardening* (Fleck and Hutchinson, 1993; Fleck et al., 1994; Fleck and Hutchinson, 1997, 2001). Under these assumptions, Fokoua et al. (2013, 2014) show, through rigorous mathematical proofs, that ductile fracture emerges as the net outcome of two competing effects: whereas the sublinear growth of the energy in the large-body limit promotes localization of deformation to failure planes, strain-gradient plasticity stabilizes this process of localization in its advanced stages, thus resulting in a well-defined specific fracture energy.

In the present work we follow a similar program for polymers. Thus, we posit that fracture in polymers results from a competition between distributed damage, due to progressive chain failure, and fractional strain-gradient elasticity. Thus, we assume that the material behavior has two components, *local* and *nonlocal*. The local behavior is characteristic of large material samples deforming uniformly and it represents the configurational statistics of a polymeric chain network in the thermodynamic limit (cf., e. g., Weiner (2002); Flory (1989)). We note that in general, damage is a time-dependent process governed by equations of evolution. In particular, for arbitrary loading paths the rate of damage can be zero below a certain threshold and non-zero only when the threshold is attained. In order to simplify the analysis, we restrict attention to monotonic and proportional loading processes for which damage accumulates continuously. We thus extend the classical network theory by assuming that the chain bonds have a finite strength. When the strength of the chain is reached, the chain is assumed to fail and to subsequently have no load-bearing capacity. In these cases, the behavior of the solid is characterized by an effective strain-energy density referred to as "deformation-theoretical" (an extensive account of deformation theory, as it applies to general inelastic solids, may be found in Martin (1975)). Therefore, this effective free energy combines the chain elasticity and the dissipation due to chain failure. We show that, for large deformations, the deformation-theoretical free energy has *zero growth*, i. e., it is bounded above and below by a constant.

Energies with sublinear growth relax to zero, i. e., allow the material to fracture with zero expenditure of energy, and thus fail to supply useful information regarding fracture properties. We assume that, in polymers undergoing fracture, this inherently unstable behavior is held in check by a second fundamental property, namely, the *fractional strain-gradient elasticity*. By fractional strain-gradient elasticity we specifically mean a generalization of conventional strain-gradient elasticity (cf., e. g., Kröner (1968); Hermann (1974); Maugin and Metrikine (2010)) in which the strain-energy density depends on fractional derivatives (cf., e. g., (Adams, 1975)) of the deformation gradient. The need to consider fractional derivatives in the definition of the

energy stems from the fact that conventional strain-gradient elasticity is too rigid to enable the type of deformations involving in the crazing mechanism and, hence, is incompatible with experimental observation. Thus, if the strain-energy density has at least linear growth in the second deformation gradient $\nabla^2 \boldsymbol{y}$, then, for all configurations of finite energy $\nabla^2 \boldsymbol{y}$ is necessarily integrable and, hence, the deformation mapping $\boldsymbol{y}$ is continuous on almost every plane by Sobolev embedding (cf., e. g., (Adams, 1975)). This continuity of $\boldsymbol{y}$, in turn, precludes the formation of the fibrils characteristic of the crazing mechanism, which necessarily entails discontinuous deformation mappings (hence leading to discontinuous displacements). By contrast, as we shall see, the use of fractional derivatives removes sufficient rigidity from conventional strain-gradient elasticity to allow for crazing deformations, thus bringing the theory within the realm of experimental observation.

In the present context, fractional strain-gradient elasticity encodes key aspects of polymer behavior, such as surface and interfacial energy, not accounted for in the local model. The fractional strain-gradient elasticity of the polymer results in deviations from volume scaling, i. e., in nonlocal behavior and size dependency, in sufficiently small material samples. Under these conditions, polymer fracture emerges as the net result of two competing effects: whereas the zero growth of the local energy promotes localization of deformation to failure planes, or crazes, fractional strain-gradient elasticity stabilizes this process of localization, thus resulting in an orderly progression towards failure and a well-defined specific fracture energy.

A principal aim of the present work is to derive rigorous optimal scaling laws for the macroscopic fracture energy from the micromechanical model just described. Such optimal scaling laws are established producing upper and lower bounds of a power-law type with matching exponents for all parameters in both bounds. In order to facilitate the analysis, we assume that the effective deformation-theoretical energy is additive in the first and second deformation-gradients, with zero growth of the former and linear growth of the latter. The specific problem considered concerns a material sample in the form of an infinite slab of finite thickness subjected to prescribed opening displacements on its two surfaces. Under these conditions, we derive optimal scaling laws for the dependence of the effective energy on cross-sectional area, micromechanical parameters, opening displacement and intrinsic length of the material. In particular, the upper bound is obtained by means of a construction that mimics, in a particular simple manner, the crazing mechanism. The scaling laws thus derived supply a rigorous link between micromechanical properties and macroscopic fracture properties of polymers. In particular, they reveal the relative roles that surface energy and chain elasticity and damage play as contributors to the specific fracture energy of the material.

The macroscopic fracture model that results from the optimal scaling analysis is characterized by a single parameter, namely, the critical energy-

release rate G_c. This simple structure greatly facilitates material characterization. By way of illustration, and in order to calibrate subsequent calculations, we estimate G_c for polyurea 1000 from the uniaxial-tension test data of Weinberg and Reppel (2013). Another appealing aspect of the macroscopic fracture model is that it is amenable to a straightforward numerical implementation based on material-point erosion (Schmidt et al., 2009; Li et al., 2012; Pandolfi and Ortiz, 2012). We demonstrate the scope of the resulting numerical model by means of an example of application: The Taylor-impact experiments of Mock *et al.* on polyurea 1000 specimens (Mock and Drotar, 2006; El Sayed et al., 2009). These simulations additionally furnish a modicum of validation of the fidelity of the failure and fracture model. Remarkably, the simulations match closely both the observed patterns of distributed damage as well as the development of discrete fractures or tears. The simulations are also in fair agreement with quantitative metrics such as the specimen length and exhibit robust convergence with respect to mesh size.

2. Theory

In this section we put forth a simple local model of bulk behavior, based on the classical statistical mechanical treatment of freely-jointed polymer chains extended to account for chain failure. We also put forth an equally simple model of nonlocal energy based on an assumption of isotropy and of linear growth of the strain-gradient elastic energy density, based on the use of fractional derivatives. Evidently, more elaborate statistical-mechanical models of polymer elasticity, failure and strain-gradient elasticity can be considered within the general framework developed here. However, simple models such as described do suffice to illustrate the general framework and enhancements of the models thereof will not be considered here. In addition, it is important to note that the optimal scaling laws derived in the sequel, which effectively bridge the micro and macroscales, do not depend on the fine details of the energy density but only on its growth properties for large deformations and deformation gradients. In this sense, the optimal scaling laws apply uniformly to classes of material models having identical growth properties and the fine details of the models can be conveniently ignored.

2.1. Local behavior

One of the simplest models of the thermoelasticity of polymers, known as the *network theory of rubber elasticity* (Weiner, 2002; Flory, 1989), regards the polymer as an amorphous network of cross-linked long-chain molecules. The chains are freely-jointed, long and far from full extension. In order to connect the behavior of the the chains to the deformation of the continuum, we assume that the cross-linking points move affinely according to the local

macroscopic deformation. In addition, the polymer is assumed to be ostensibly incompressible at the macroscale. The standard analysis (cf., e. g., Weiner (2002)) then gives the free-energy density per unit volume as

$$A_{\rm loc}(\boldsymbol{F}) = \begin{cases} nk_BTK_{IJ}C_{IJ}, & \text{if } \det(\boldsymbol{F}) = 1, \\ +\infty, & \text{otherwise,} \end{cases} \tag{1}$$

where n is the number of chains per unit volume, $\boldsymbol{F}$ is the local deformation gradient, $\boldsymbol{C} = \boldsymbol{F}^T\boldsymbol{F}$ is the right Cauchy-Green deformation tensor, n is the number of chains per unit volume, k_B is Bolzmann's constant, T is the absolute temperature and incompressibility, $\det(\boldsymbol{F}) = 1$ is enforced through a hard constraint. In addition, the structure tensor $\boldsymbol{K}$ follows as

$$K_{IJ} = \frac{3l^2}{b^2}\int_{S^2} p(\boldsymbol{\xi})\xi_I\xi_J\, d\Omega, \tag{2}$$

where b is the link length, l is the end-to-end distance of the chains, ξ is the chain end-to-end unit vector, $p(\boldsymbol{\xi})$ is the fraction of chains in the ensemble having a chain end-to-end unit vector $\boldsymbol{\xi}$, S^2 is the unit sphere and $d\Omega$ is the element of solid angle. The density $p(\boldsymbol{\xi})$ is subject to the normalization condition

$$\int_{S^2} p(\boldsymbol{\xi})\, d\Omega = 1. \tag{3}$$

For an isotropic distribution of chains, $p = 1/4\pi$, we have

$$\int_{S^2} p(\boldsymbol{\xi})\xi_I\xi_J\, d\Omega = \frac{1}{3}\delta_{IJ}, \tag{4}$$

and (2) reduces to

$$K_{IJ} = \frac{l^2}{b^2}\delta_{IJ}, \tag{5}$$

whence (1) in turn reduces to the strain-energy density of a neo-Hookean solid.

We note that, in principal directions, $\boldsymbol{C} = \mathrm{diag}(\lambda_1^2, \lambda_2^2, \lambda_3^2)$ and

$$K_{IJ}C_{IJ} = K_1\lambda_1^2 + K_2\lambda_2^2 + K_3\lambda_3^2, \tag{6}$$

where

$$K_I = \frac{3l^2}{b^2}\int_{S^2} p(\boldsymbol{\xi})\xi_I^2\, d\Omega. \tag{7}$$

Furthermore, by the arithmetic mean-geometric inequality and incompressibility we have

$$K_1\lambda_1^2 + K_2\lambda_2^2 + K_3\lambda_3^2 \geq 3[(K_1\lambda_1^2)(K_2\lambda_2^2)(K_3\lambda_3^2)]^{1/3} = 3(K_1K_2K_3)^{1/3}. \tag{8}$$

Combining these inequalities we have

$$A_{\rm loc}(\boldsymbol{F}) \geq 3(K_1K_2K_3)^{1/3}nk_BT \equiv A_0. \tag{9}$$

For an isotropic polymer we additionally have $K_1 = K_2 = K_3 = l^2/b^2$ and

$$A_0 = \frac{3nk_BTl^2}{b^2} = A_{\rm loc}(\boldsymbol{I}). \tag{10}$$

Next, we proceed to extend the classical model of polymer elasticity just described to account for damage in the form of broken chains. Suppose that chains break when the end-to-end vector attains a critical stretch $\lambda_c > 1$, and that the failure of one chain costs energy in the amount E_b. Thus, according to this criterion a previously intact chain of end-to-end direction $\boldsymbol{\xi}$ fails when

$$\boldsymbol{\xi}^T\boldsymbol{C}\boldsymbol{\xi} = \lambda_c^2. \tag{11}$$

We can describe the state of damage of the network by means of the damage distribution function

$$D(\boldsymbol{\xi}) = \begin{cases} 0, & \text{if the chains of end-to-end direction } \boldsymbol{\xi} \text{ are broken,} \\ 1, & \text{if the chains of end-to-end direction } \boldsymbol{\xi} \text{ are unbroken.} \end{cases} \tag{12}$$

The corresponding structure constant now depends on the state of damage as

$$K_{IJ}(D) = \frac{3l^2}{b^2}\int_{S^2} p(\boldsymbol{\xi})D(\boldsymbol{\xi})\xi_I\xi_J\, d\Omega, \tag{13}$$

and the free-energy density takes the form

$$A_{\rm loc}(\boldsymbol{F}, D) = \begin{cases} nk_BTK_{IJ}(D)C_{IJ} + nf(D), & \text{if } \det(\boldsymbol{F}) = 1, \\ +\infty, & \text{otherwise,} \end{cases} \tag{14}$$

where

$$f(D) = \frac{3E_bl^2}{b^2}\int_{S^2} p(\boldsymbol{\xi})(1 - D(\boldsymbol{\xi}))\, d\Omega, \tag{15}$$

is the total energy dissipated through chain breaking. For arbitrary local deformation histories $\boldsymbol{C}(t)$, the corresponding evolution $D(\boldsymbol{\xi}, t)$ of the damage distribution function is governed by the rate-independent kinetics

$$D(\boldsymbol{\xi}, t) = \begin{cases} 1, & \text{if } \boldsymbol{\xi}^T\boldsymbol{C}(t')\boldsymbol{\xi} \le \lambda_c^2,\ \forall t' \le t, \\ 0, & \text{otherwise.} \end{cases} \tag{16}$$

However, for present purposes, it suffices to confine attention to monotonic deformation processes such that the stretch $\sqrt{\boldsymbol{\xi}^T\boldsymbol{C}(t)\boldsymbol{\xi}}$ is monotonically increasing in all directions. Indeed, in polymers undergoing crazing under predominantly tensile loading, the deformations leading to failure may be reasonably approximated as being monotonic. Under these conditions, the damage distribution function is determined as a function of $\boldsymbol{C}$, namely,

$$D(\boldsymbol{\xi}, \boldsymbol{C}) = \begin{cases} 1, & \text{if } \boldsymbol{\xi}^T\boldsymbol{C}\boldsymbol{\xi} \le \lambda_c^2, \\ 0, & \text{otherwise.} \end{cases} \tag{17}$$

The structure tensor and the dissipated energy follow likewise as a direct function of $\boldsymbol{C}$, namely,

$$K_{IJ}(\boldsymbol{C}) = \frac{3l^2}{b^2} \int_{S^2} p(\boldsymbol{\xi}) D(\boldsymbol{\xi}, \boldsymbol{C}) \xi_I \xi_J \, d\Omega \tag{18}$$

and

$$f(\boldsymbol{C}) = \frac{3E_b l^2}{b^2} \int_{S^2} p(\boldsymbol{\xi})(1 - D(\boldsymbol{\xi}, \boldsymbol{C})) \, d\Omega, \tag{19}$$

The corresponding free-energy density takes on the deformation-theoretical form

$$W_{\mathrm{loc}}(\boldsymbol{F}) = \begin{cases} nk_B T K_{IJ}(\boldsymbol{C}) C_{IJ} + nf(\boldsymbol{C}), & \text{if } \det(\boldsymbol{F}) = 1, \\ +\infty, & \text{otherwise.} \end{cases} \tag{20}$$

Thus, for as long as the deformation history remains monotonic, the free-energy density of the polymer is indistinguishable from that of a thermoelastic solid.

2.2. Growth properties of the deformation-theoretical strain-energy density

In order to make contact with macroscopic fracture properties, the growth properties of the deformation-theoretical free-energy density $W_{\mathrm{loc}}(\boldsymbol{F})$, eq. (20), are of critical importance, cf. Section 3. Therefore, we proceed to ascertain the growth characteristics of $W_{\mathrm{loc}}(\boldsymbol{F})$ for large $\boldsymbol{C}$.

2.2.1. Upper bound

We begin by noting that

$$\begin{aligned} K_{IJ}(\boldsymbol{C}) C_{IJ} &= \frac{3l^2}{b^2} \int_{S^2} p(\boldsymbol{\xi}) D(\boldsymbol{\xi}, \boldsymbol{C}) \boldsymbol{\xi}^T \boldsymbol{C} \boldsymbol{\xi} \, d\Omega \\ &\leq \frac{3l^2}{b^2} \int_{S^2} p(\boldsymbol{\xi}) \lambda_c^2 \, d\Omega = \frac{3l^2 \lambda_c^2}{b^2}. \end{aligned} \tag{21}$$

This estimate supplies a bound for the first term in $W_{\mathrm{loc}}(\boldsymbol{F})$, or strain-energy term. In order to estimate the damage energy we note that

$$f(\boldsymbol{C}) = \frac{3E_b l^2}{b^2} \int_{S^2} p(\boldsymbol{\xi})(1 - D(\boldsymbol{\xi}, \boldsymbol{C})) \, d\Omega \leq \frac{3E_b l^2}{b^2} \int_{S^2} p(\boldsymbol{\xi}) \, d\Omega = \frac{3E_b l^2}{b^2}. \tag{22}$$

Combining the above estimates we finally obtain the constant upper bound

$$W_{\mathrm{loc}}(\boldsymbol{F}) \leq 3(E_b + k_B T \lambda_c^2) \frac{l^2}{b^2}. \tag{23}$$

2.2.2. Lower bound

Next we proceed to bound $W_{\rm loc}(\boldsymbol{F})$ from below for large $\boldsymbol{F}$. Evidently, $W_{\rm loc}(\boldsymbol{F})$ is, at least, the damage energy, i. e.,

$$W_{\rm loc}(\boldsymbol{F}) \geq nf(\boldsymbol{C}). \tag{24}$$

In principal coordinates of $\boldsymbol{C}$ we have, from (17),

$$1 - D(\boldsymbol{\xi}, \boldsymbol{C}) = \begin{cases} 1, & \text{if } \lambda_1^2\xi_1^2 + \lambda_2^2\xi_2^2 + \lambda_3^2\xi_3^2 \geq \lambda_c^2, \\ 0, & \text{otherwise.} \end{cases} \tag{25}$$

where $(\lambda_1, \lambda_2, \lambda_3)$ are the principal stretches. Suppose that $\lambda_1 \geq \lambda_2 \geq \lambda_3$ and $|\boldsymbol{F}| = \sqrt{\lambda_1^2 + \lambda_2^2 + \lambda_3^2} \to +\infty$ while $\lambda_1\lambda_2\lambda_3 = 1$. Suppose, in addition, that $\operatorname{essinf}(p) \geq p_{\min} > 0$, i. e., the chain density is positive in all chain directions. Then,

$$1 - D(\boldsymbol{\xi}, \boldsymbol{C}) \geq g(\boldsymbol{\xi}, \boldsymbol{C}) = \begin{cases} 1, & \text{if } \lambda_1^2\xi_1^2 \geq \lambda_c^2, \\ 0, & \text{otherwise,} \end{cases} \tag{26}$$

and

$$f(\boldsymbol{C}) \geq = \frac{3E_b l^2}{b^2} \int_{S^2} p(\boldsymbol{\xi}) g(\boldsymbol{\xi}, \boldsymbol{C})\, d\Omega = \frac{3E_b l^2}{b^2} \int_{S^2 \setminus \{|\xi_1| \geq \lambda_c/\lambda_1\}} p(\boldsymbol{\xi})\, d\Omega, \tag{27}$$

and as $\lambda_1 \to +\infty$,

$$W_{\rm loc}(\boldsymbol{F}) \geq 4\pi p_{\min} n \frac{3E_b l^2}{b^2}, \tag{28}$$

which establishes a constant lower bound for the deformation-theoretical strain-energy density. The bound simply expresses the fact that, in the limit under consideration, all chains are likely to be broken at sufficiently large deformations.

2.2.3. Illustrative examples

The preceding bounds show that the deformation-theoretical strain-energy density $W_{\rm loc}(\boldsymbol{F})$ has zero growth, i. e., saturates to a constant, for sufficiently large deformations. Correspondingly, the first Piola-Kirchhoff stress decays to zero in the same limit. This behavior is illustrated in Fig. 3 through the example of a polymer deformed in uniaxial tension, $\boldsymbol{F} = \operatorname{diag}(\lambda^{-1/2}, \lambda^{-1/2}, \lambda)$. The polymer is isotropic, $p = 1/4\pi$ and the chains fail at a critical stretch $\lambda_c = 2$. Fig. 3a corresponds to a bond-binding energy $E_b/k_BT = 2$, or strong chains, whereas Fig. 3b corresponds to a bond-binding energy $E_b/k_BT = 0.2$, or weak chains. The zero growth of the deformation-theoretical strain-energy for large deformations is evident in both cases. However, the saturation value of the energy is attained from below in the case of strong chains and from above in the case of weak chains. This difference of behavior is expected,

strong chains (respectively, weak chains) dissipate large (respectively, small) amounts of energy upon failure. We note that the strong chain condition $^{E_b}/_{k_BT} > 1$ (respectively, weak chain condition $^{E_b}/_{k_BT} < 1$) correspond to the range $E_b > A_0$ (respectively, $E_b < A_0$).

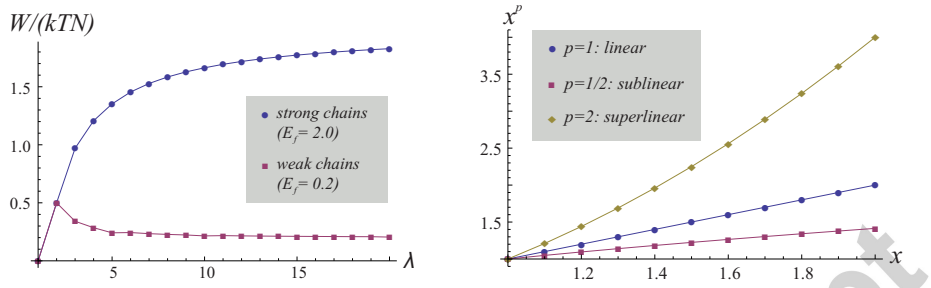

(a) (b)

Figure 3: a) Deformation-theoretical strain-energy density $W_{\text{loc}}(\boldsymbol{F})$ for an isotropic polymer deforming in uniaxial tension, $\boldsymbol{F} = \text{diag}(\lambda^{-1/2}, \lambda^{-1/2}, \lambda)$. The chains fail at a critical stretch $\lambda_c = 2$ and have bond-binding energies of $^{E_b}/_{k_BT} = 2$ and $^{E_b}/_{k_BT} = 0.2$, respective. b) Schematic of functions with linear, sublinear and superlinear growth.

2.3. Nonlocal regularization

Mathematically, energies exhibiting sublinear growth[1] may be expected to relax to zero via strain localization to small volumes, a degenerate limit that provides no useful information about fracture properties. Our model rests on the assumption that this unstable behavior is stabilized by nonlocal or strain-gradient effects. For metals, this property has been extensively investigated and demonstrated by means of torsion tests in wires Fleck et al. (1994), nanoindentation Nix and Gao (1998); Xue et al. (2000); Huang et al. (2000), and by other means. Specifically, for fixed local deformation, the energy density of solids is often observed to be an increasing function of the local strain gradient, or the second deformation gradient. This property results in deviations from volume scaling, i. e., in nonlocal behavior and size dependency, in sufficiently small material samples.

A first candidate means of accounting for strain-gradient effects, along the lines of Fokoua et al. (2013, 2014), is provided by strain-gradient elasticity (cf., e. g., Kröner (1968); Hermann (1974); Maugin and Metrikine (2010)). This framework consists of assuming an extended deformation-theoretical free-energy density of the form $W(\boldsymbol{F}, \nabla\boldsymbol{F})$ with the limiting

[1] Cf. Fig. 3b for a schematic illustration of functions exhibiting linear, sublinear and superlinear growth

property that

$$W(\boldsymbol{F}, \boldsymbol{0}) = W_{\text{loc}}(\boldsymbol{F}), \tag{29}$$

i. e., the local deformation-theoretical free-energy density $W_{\text{loc}}(\boldsymbol{F})$ is recovered for uniform deformations. The precise form of $W(\boldsymbol{F}, \nabla \boldsymbol{F})$ is unknown for most polymers. Conveniently, for purposes of optimal scaling only the growth properties of $W(\boldsymbol{F}, \cdot)$ are required. A hint of the likely growth properties of $W(\boldsymbol{F}, \cdot)$ is provided by observations of sharp twin interfaces in crystalline polymers deformed in shear (Agar et al., 1959; Reneker and Geil, 1960; Geil, 1963; Kiho et al., 1964; Keller, 1968; Kovacs et al., 1969; Wittmann and Kovacs, 1970; Pradère et al., 1988; Alcazar et al., 2006). Atomistic simulations of shear deformation in polymers also supply evidence of lamination and of the development of sharp interfaces (cf., e. g., Fortunelli et al. (2004); Fortunelli and Ortiz (2007) and references therein). Mathematically, sharp interfaces can only arise in strain-gradient elasticity if $W(\boldsymbol{F}, \nabla \boldsymbol{F})$ exhibits linear growth with respect to $\nabla \boldsymbol{F}$.

However, the strain-gradient framework just described has the deficiency of not allowing for crazing and, hence, is incompatible with experimental observation. Thus, if $W(\boldsymbol{F}, \nabla \boldsymbol{F})$ has linear growth in $\nabla \boldsymbol{F}$, then, for a configuration of finite energy, $\nabla^2 \boldsymbol{y}$ is integrable and, hence, $\boldsymbol{y}$ is continuous (Adams, 1975). The continuity of $\boldsymbol{y}$, in turn, precludes the formation of the fibrils characteristic of the crazing mechanism. We note that, by contrast, the void-sheet mechanism characteristic of ductile fracture in metals is compatible with strain-gradient plasticity (cf. Fokoua et al. (2013, 2014)).

In this work, we remedy this deficiency of conventional strain-gradient elasticity by assuming instead an extended deformation-theoretical free-energy density with growth controlled by a fractional Sobolev seminorm $|D\boldsymbol{y}|_{W^{\sigma,1}(\Omega)}$ of the deformation gradient, with $0 < \sigma < 1$ (cf. Adams (1975) for a discussion of fractional Sobolev spaces and for explicit formulas for the computation of the corresponding norms). We remark that $|D\boldsymbol{y}|_{W^{\sigma,1}(\Omega)}$ still implies linear growth of the nonlocal energy density but may be regarded as the integral of a fractional derivative $|D^{1+\sigma}\boldsymbol{y}|$ of the deformation gradient $D\boldsymbol{y}$. This assumption effectively weakens the strain-gradient effect sufficiently to allow for crazing deformations. In particular, we show in the sequel that, in fractional strain-gradient solids, the crazing mechanism indeed delivers an optimal bound of the energy, in the sense of optimal scaling.

3. Optimal scaling and specific fracture energy

We recall (Kohn and Müller, 1992, 1994; Choksi et al., 1999) that an energy functional $E(\cdot, \epsilon_1, \ldots, \epsilon_N)$, depending on N parameters $(\epsilon_1, \ldots, \epsilon_N)$, is said to exhibit optimal scaling if it satisfies matching upper and lower

bounds of the form

$$C_L\epsilon_1^{\alpha_1}\dots\epsilon_N^{\alpha_N} \leq \inf E(\cdot,\epsilon_1,\dots,\epsilon_N) \leq C_U\epsilon_1^{\alpha_1}\dots\epsilon_N^{\alpha_N}, \tag{30}$$

where $C_L > 0$ and $C_U > 0$ are constants and the exponents $(\alpha_1,\dots,\alpha_N)$ are identical in both the lower and the upper bounds. The constants C_L and C_U appearing in (30) give rigorous lower and upper bounds, and are not uniquely determined. Their precise value depends on the strategy of proof chosen, often there is a tradeoff between simplicity of the argument and the distance between C_L and C_U. By contrast, the exponents $(\alpha_1,\dots,\alpha_N)$ are uniquely determined and represent intrinsic properties of the problem considered.

Rigorous optimal scaling laws for fractional strain-gradient solids with constant-linear energy growth of the type described in the foregoing have been derived by Conti and Ortiz (2014). Here we summarize the main arguments underlying the derivation of the optimal scaling laws and discuss their connection to fracture. The optimal scaling laws show that the materials under consideration do indeed fail by fracture, i. e., by localization of deformation to a plane, and that the fracture process requires the expenditure of a well-defined fracture energy, or critical energy-release rate, G_c.

3.1. Problem formulation

Based on the considerations in the preceding section, we shall assume that the deformation-theoretical free-energy $E(\boldsymbol{y})$ obeys the following growth property

$$\int_\Omega W_L(\nabla\boldsymbol{y})\,dx + k_L\ell^\sigma|D\boldsymbol{y}|_{W^{\sigma,1}(\Omega)} \leq E(\boldsymbol{y}), \tag{31a}$$

$$E(\boldsymbol{y}) \leq \int_\Omega W_U(\nabla\boldsymbol{y})\,dx + k_U\ell^\sigma|D\boldsymbol{y}|_{W^{\sigma,1}(\Omega)}, \tag{31b}$$

where $0 < k_L \leq k_U < +\infty$ are constants,

$$W_L(\boldsymbol{F}) = \begin{cases} \min\{k_L, nk_BTK_{IJ}C_{IJ}\}, & \text{if } \det(\boldsymbol{F}) = 1, \\ +\infty, & \text{otherwise,} \end{cases} \tag{32}$$

and

$$W_U(\boldsymbol{F}) = \begin{cases} \min\{k_U, nk_BTK_{IJ}C_{IJ}\}, & \text{if } \det(\boldsymbol{F}) = 1, \\ +\infty, & \text{otherwise,} \end{cases} \tag{33}$$

are truncated local energy densities, $\ell > 0$ is an *intrinsic* or *characteristic length*, and $|D\boldsymbol{y}|_{W^{\sigma,1}(\Omega)}$ is a fractional Sobolev seminorm (cf. Appendix A for a definition). Here the structure tensor K_{IJ} corresponds to the undamaged material, as was defined in (2). In addition, the density $p(\boldsymbol{\xi})$ is assumed to be such that the minimum of W_U and W_L is attained at the identity. We then denote

$$A_0 = \min W_U = \min W_L = W_U(\boldsymbol{I}) = W_L(\boldsymbol{I}). \tag{34}$$

For example, the isotropic density $p(\boldsymbol{\xi}) = 1/4\pi$ has the property (34) and A_0 is given by (10). We note that the analysis is meaningful only if the truncated energy densities are not constant, resulting in the constraint $A_0 < k_L \leq k_U$ on the parameters. We also emphasize that the deformation-theoretical free-energy $E(\boldsymbol{y})$ itself need not be of the form expressed by the bounds (31), which merely define the growth properties of the energy.

In order to make connection with fracture, we specifically consider periodic deformations of a slab of thickness $2H$ occupying the domain $\{|x_3| \leq H\}$ subject to prescribed opening displacements δ on its surfaces. We identify a periodic unit cell $\Omega = [0, L]^2 \times (-H, H)$ and describe the deformation of the slab by means of a $[0, L]$-periodic deformation mapping $\boldsymbol{y} : \Omega \to \mathbb{R}^3$ subject to the constraint of volume conservation in Ω and to displacement boundary conditions

$$y_3(x_1, x_2, -H) = -H - \delta, \tag{35a}$$
$$y_3(x_1, x_2, H) = H + \delta, \tag{35b}$$

with $(x_1, x_2) \in [0, L]^2$. The aim of the analysis is to derive optimal, or matching, upper and lower bounds for the energy of the slab as a function of L, ℓ and δ.

3.2. Upper bound

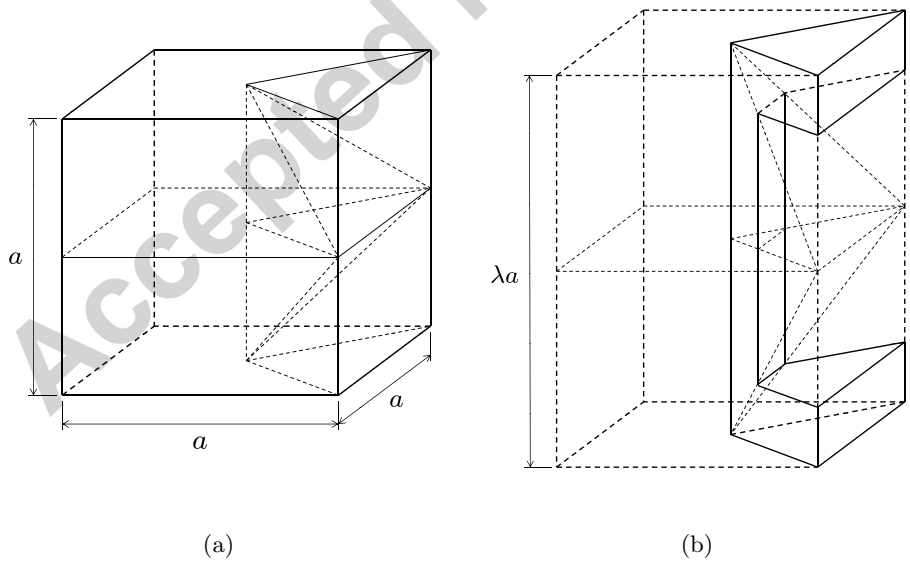

(a) (b)

Figure 4: Schematic of deformation mapping used in the upper bound construction. a) Reference configuration. b) Deformed configuration.

Owing to the minimum principle underlying deformation theory of plasticity, an upper bound can be obtained simply by direct evaluation of the energy for an admissible test mapping. A deformation mapping which describes, in a simple manner, the process of crazing is given in the appendix and shown schematically in Fig. 4. The deformation is localized to the layer $(0, L)^2 \times (-a, a) \subset \Omega$ and, elsewhere, the slab undergoes a rigid translation through the prescribed opening displacement $\pm\delta$. The layer $(0, L)^2 \times (-a, a)$ is then subdivided into $\sim (L/a)^2$ identical cubes of size a. Fig. 4 specifically depicts the deformation in one of the cubes. The deformation is everywhere volume preserving and results in the formation of a fibril along the vertical axis of the cube by means a process of cavitation from the four boundary segments on the symmetry plane of the cube. Furthermore, the deformation mapping $\nabla \boldsymbol{y}$ is integrable, though the second deformation gradient $\nabla^2 \boldsymbol{y}$ is not, as expected from the discontinuous nature of crazing on almost every plane. As noted above, this lack of integrability results in infinite energies in solids obeying strain-gradient elasticity. We relax this excessive rigidity of strain-gradient elasticity by assuming that the solid obeys fractional strain-gradient elasticity instead.

Inserting the deformation mapping (A.14) and (A.15) into (31), lengthy but straightforward calculations give an energy bound dependent on L, ℓ, δ and a,

$$E(\boldsymbol{y}) \leq 2L^2 A_0 H + 2k_U L^2 a + c k_U L^2 \ell^\sigma \frac{\delta}{a^\sigma}\,, \tag{36}$$

where c is a positive constant which depends on the details of the construction. Further minimizing the bound with respect to a results in $a \sim \delta^{1/(1+\sigma)} \ell^{\sigma/(1+\sigma)}$ and gives an upper bound of the form

$$E - 2L^2 A_0 H \leq c_U k_U L^2 \ell^{\frac{\sigma}{1+\sigma}} \delta^{\frac{1}{1+\sigma}} \tag{37}$$

We note that the bound takes the form of a power law in the variables L, ℓ and δ. The constant $2A_0 L^2 H$ is an inconsequential datum that reflects the normalization of the energy density.

3.3. Lower bound

Evidently, every choice of test deformation mapping produces an upper bound of the energy via (31). However, Conti and Ortiz (2014) have shown, through arguments of mathematical analysis of a somewhat technical nature, that the upper bound (37) is indeed optimal, in the sense that there exists a matching lower bound of the form

$$c_L k_L L^2 \ell^{\frac{\sigma}{1+\sigma}} \delta^{\frac{1}{1+\sigma}} \leq E - 2L^2 A_0 H, \tag{38}$$

with identical exponents of L, ℓ and δ. The key idea is to combine the fact that the local energy can only be small if the deformation is concentrated on

a small part of the domain with a Poincaré inequality to control the L^1 norm of $D\boldsymbol{y}$ by its $W^{\sigma,1}$ norm. We note that, whereas the constants c_L and c_U may be lax, owing, e. g., to the simplicity of the test deformation mapping used in the upper bound construction, the scaling exponents are hard and precise predictions of the theory. We also note that, for the topological reasons discussed earlier, the constants necessarily blow up as σ approaches 1 from below, i. e., in the limit of conventional strain-gradient elasticity.

3.4. Relation to fracture

Considered jointly, the bounds (37) and (38) yield the optimal scaling law

$$c_L k_L L^2 \ell^{\frac{\sigma}{1+\sigma}} \delta^{\frac{1}{1+\sigma}} \leq E_{\min} - 2A_0 L^2 H \leq c_U k_U L^2 \ell^{\frac{\sigma}{1+\sigma}} \delta^{\frac{1}{1+\sigma}}. \tag{39}$$

We note that the bounds (39) scale with the in-plane area L^2 and are independent of the thickness $2H$ of the slab. This type of scaling is characteristic of *fracture processes*, in which the deformation is concentrated in the neighborhood of a fracture surface and the energy scales with the area of the surface. In particular, the specific energy per unit area

$$\Phi = \frac{E_{\min} - 2A_0 L^2 H}{L^2} \tag{40}$$

is bounded and independent of the thickness $2H$ of the slab. The bounds (39) can be recast in terms of this specific energy per unit area as

$$c_L k_L \ell^{\frac{\sigma}{1+\sigma}} \delta^{\frac{1}{1+\sigma}} \leq \Phi \leq c_U k_U \ell^{\frac{\sigma}{1+\sigma}} \delta^{\frac{1}{1+\sigma}}. \tag{41}$$

Fix now ℓ and regard the specific energy per unit area as a function $\Phi(\delta)$ of the opening displacement. By the work-energy theorem the corresponding applied normal traction then follows as

$$\sigma = \frac{\partial \Phi}{\partial \delta} = \sigma(\delta). \tag{42}$$

This relation may be regarded as a cohesive law that relates opening displacement δ and traction σ.

We recall that the attainment of a critical value of Rice's J-integral (Rice, 1968) provides a standard and widely used non-linear fracture criterion with several attractive properties (cf., e. g., Hutchison (1979); Kanninen and Popelar (1985) for reviews): i) For elastic materials J coincides with G, the elastic energy-release rate; ii) for power-law small-strain plastic behavior, J determines the strength of the HRR singular field (Hutchinson, 1968; Rice and Rosengren, 1968) at the crack tip; and iii) it can be evaluated experimentally in a convenient manner. For an otherwise elastic material obeying a cohesive fracture law, an application of Rice's J-integral (Rice, 1968) gives the plane-strain critical energy-release rate at crack-growth initiation as

$$G_c = \int_0^{+\infty} \sigma(\delta)\, d\delta = \Phi(+\infty) - \Phi(0). \tag{43}$$

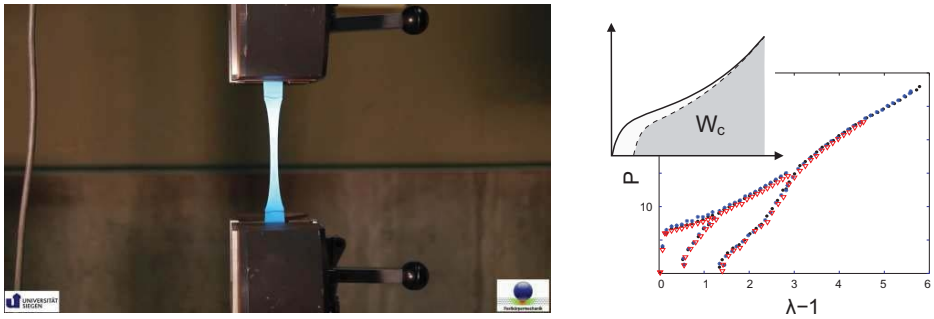

Figure 5: Uniaxial tension test of polyurea 1000 with feed of 2mm/s (Reppel et al., 2012). Left: Thin-strip specimen stretched quasistatically up to failure. Right: Determination of the elastic strain energy density by data reduction.

Inserting the upper bound (41) into (43) we find that the integral is indeed convergent at the origin, and a void nucleation model is not required in order to ensure the boundedness of G_c. By contrast, inserting the lower bound (41) into (43) the same integral diverges at infinity, i. e., it predicts an infinite G_c. In order to eliminate this divergence we may introduce a cut-off δ_c, representing a critical opening displacement at crack-growth initiation, and write

$$G_c = \int_0^{\delta_c} \sigma(\delta)\, d\delta = \Phi(\delta_c) - \Phi(0). \tag{44}$$

In the present context, δ_c may conveniently be identified with the chain length of the polymer, on the grounds that failure must occur when the chains are stretched beyond their fully-stretched length.

Inserting the bound (41) into (44) we obtain

$$c_L k_L \ell^{\frac{\sigma}{1+\sigma}} \delta_c^{\frac{1}{1+\sigma}} \leq G_c \leq c_U k_U \ell^{\frac{\sigma}{1+\sigma}} \delta_c^{\frac{1}{1+\sigma}}, \tag{45}$$

which supplies bounds for G_c as a function of the internal length ℓ, the critical opening displacement δ_c and the material constants k_L and k_U. The bounds (45) supply a link between independently measurable material and fracture properties, and thus open the theory to experimental calibration.

4. Supporting microscopy and experimental calibration

The macroscopic fracture model that results from the optimal scaling analysis is solely characterized by the critical energy-release rate G_c. In elastic fracture mechanics, G_c sets a threshold value of the elastic energy-release rate for crack propagation. For highly stretched rubbery materials, Rivlin and Thomas (1953) argued that G_c provides a measure of the resistance to tearing of the material. From dimensional considerations, we

have

$$G_c = l_c\, W_c \tag{46}$$

where l_c is the width of the process zone contributing to the rupture process, $W(\lambda)$ is the elastic strain-energy density as a function of the applied stretch λ and $W_c \equiv W(\lambda_c)$ is elastic strain-energy density at rupture. We note that the process-zone width l_c and the rupture stretch λ_c depend on the geometry of the specimen and, therefore, do not represent material properties. By contrast, G_c is expected to be geometry-independent and, thus, represent a material property.

In this work, the specimens employed for the determination of the critical energy-release rate G_c of polyurea 1000 were dog-bone-shaped thin strips under tension, Fig. 5a. Since we specifically investigated tear resistance under monotonic loading, the specimens were not preconditioned against the Mullins effect. Instead we accounted for the inelastic deformation within the specimen, which in turn was determined by stepwise loading and unloading of the sample. This process is illustrated by Fig. 5b, which shows the measured nominal stress *vs.* stretch curve of a specimen stretched to 150% and to 350%, followed by full unloading, and subsequently re-loaded to rupture. Based on the these loading-unloading data, the extent of energy dissipation up to rupture may be estimated. The remaining energy density supplies the requisite elastic strain-energy density to be used in (46).

Given the state of plane stress of the specimen, we assume that the width l_c of the process zone at rupture is of the order of the width of the specimen (cf., e. g., Hutchison (1979) and Kanninen and Popelar (1985) for discussions of fracture under plane-stress conditions). This identification gives $l_c = 1.15$mm. We additionally measure $W_c = 38.2\,\mathrm{MPa}$ for polyurea 1000 specimens of that width. The critical energy-release rate then follows from (46) as $G_c = 44\,\mathrm{kJ/m^2}$. This value is employed in the numerical Taylor-anvil test simulations presented in Section 5. Compared to other polymers, with typical critical energy-release rates in the range $1 - 10\,\mathrm{kJ/m^2}$ (Alger, 1997), the value of G_c thus obtained is relatively high. This high value is indeed consistent with the exceptional stretchability and tear resistance of polyurea 1000, properties that in turn render it attractive as a coating material. The close agreement between the numerical results of Section 5 and the corresponding test data lend additional support to the data-reduction procedure just described.

Virgin and post-mortem fractographic analyses of the failure surface reveal insight into the micromechanisms of fracture. In its as-received condition, the polyurea 1000 material used in tests had a porosity of about 50 voids/mm^2 with diameters in the range of $10 - 30\ \mu m$, Fig. 1a. Upon deformation, the voids grow, fibrils rupture and a large number of new voids nucleate. The void multiplication is clearly evident in post-mortem fractographs of failure planes, which show considerable dimpling. Counting the

density of dimples gives a porosity of 97 voids/mm^2, with some dimple diameters in excess of 200 μm, Fig. 1b. The complex interplay between void nucleation and growth, failed fibrils and rupture is clearly evident from the figures.

5. Taylor-anvil tests

We proceed to demonstrate the range and fidelity of the damage and fracture criterion formulated in the foregoing by means of an example of application: The Taylor-impact experiments of Mock *et al.* Mock and Drotar (2006) on polyurea 1000 specimens. The tests were performed at the Research Gas Gun Facility at the Naval Surface Warfare Center (Dahlgren Division). Cylindrical specimens of polyurea 1000 were driven into a metal anvil at different impact speeds, cf. Table 1. Fig. 6 shows a sequence of specimen snapshots during impact for an impact velocity of $v = 245$ m/s. The large deformations undergone by the specimen are evident from the figure. At sufficiently large impact velocities, the specimen is observed to petal as a result of the development of radial cracks or tears. Post-mortem examination of the specimens also reveals extensive distributed damage in the vicinity of the contact surface. The Taylor-impact experiments thus furnish a representative example of application as well as an exacting validation of the theory.

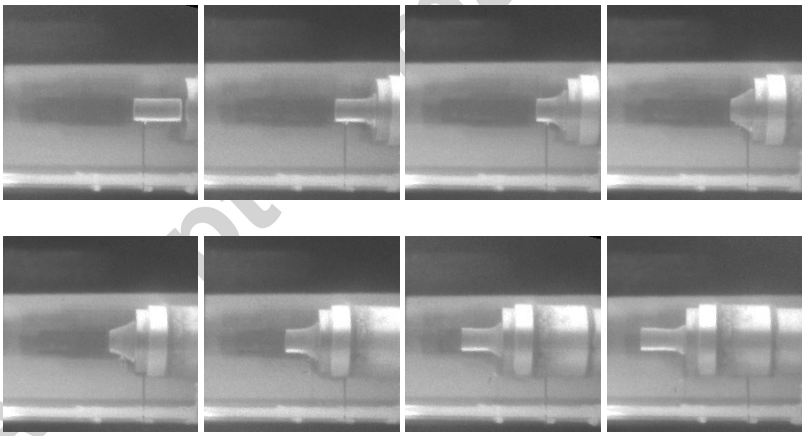

Figure 6: Taylor anvil test of polyurea 1000 rod. Experiments performed by Mock et al. at NSWC. $R_0 = 6.29603$ mm, $L_0 = 25.7353$ mm and $v = 245$ m/s.

In calculations we account for the viscoelastic behavior of polyurea by means of a standard Prony series as characterized experimentally by (Zhao et al., 2007; Knauss and Zhao, 2007). The quasistatic response of the material is additionally described by a simple neo-Hookean model. In the presence of viscoelastic and other dissipative mechanisms, the variational

Table 1: Taylor anvil test cases.

	Velocity [m/s]	Initial length [mm]	Initial diameter [mm]
Case I	245.759	25.73528	12.59205
Case II	332.047	25.60828	12.61491
Case III	424.413	25.76068	12.61745

formulation underpinning the derivation of the optimal scaling laws, and the corresponding micro-to-macro transition formulated in Section 3, is recovered through time-discretization using variational constitutive updates (Ortiz and Stainier, 1999). These updates effectively reduce the incremental problem to the minimization of an effective energy that accounts for both elastic energy and dissipation.

The integration of the equations of motion is carried out by means of the *Optimal Transportation Meshfree* (OTM) method (Li et al., 2010). The OTM method combines max-ent mesh-free interpolation (Arroyo and Ortiz, 2006) with material point sampling and supplies variational time integrators with exact conservation properties. We account for damage and fracture by means of material-point *eigenerosion*, an averaged material-point erosion scheme that is known to converge to Griffith fracture, with critical energy-release rate G_c, in the limit of zero mesh size (Schmidt et al., 2009). In this scheme, the energy-release rate G attendant to the failure of a material point is estimated by a local energy-averaging procedure, and material points are failed when G exceeds the critical energy-release rate G_c. Because the calculation of the effective energy-release rate at a material point is carried out within a local neighborhood of the point and requires no explicit representation of the crack, the implementation of the material-point failure scheme is straightforward. Implementational details and performance analysis of the eigenerosion scheme may be found in (Li et al., 2012; Pandolfi and Ortiz, 2012).

Figs. 7–9 show snapshots from simulations at the three different impact speeds under consideration. At the smallest impact velocity of $v = 245$ m/s, the specimen undergoes large deformations before rebounding but no radial cracks or tears develop. By contrast, incipient radial tearing is clearly evident at the intermediate impact velocity of $v = 332$ m/s, Fig. 8, whereas extensive petalling is predicted at the highest impact velocity of $v = 424$ m/s, Fig. 9. Remarkably, the radial tears retract almost entirely upon rebound and the specimens appear outwardly intact, as observed experimentally.

Figs.10–12 depict the state of damage in the recovered specimens at the three different speeds as computed and as observed post-mortem in tests. The experimental figures show the recovered specimens after impact, wherein the extent and distribution of damage can be clearly discern optically. The figures from simulations map the final state of damage by showing

the failed material points as black dots in the reference configuration. In all three comparisons, the simulations qualitatively capture the damage distribution within the specimen. At the lowest speed, Fig. 10, the specimen is predicted to undergo limited damage and cracking in the vicinity of the impact surface, in keeping with experimental observation. At the intermediate speed, Fig. 11, the simulations predict significant distributed damage near the impact surface, in good agreement with experiment. In the simulations, the impact surface additionally undergoes incipient radial cracking, also in agreement with observation. Finally at the largest speed, Fig. 12, both experiments and simulations reveal severe distributed damage over a large fraction of the specimen and the impact surface splits into well-defined radial cracks or tears. The ability of a simple single-parameter model to qualitatively capture both patterns of distributed damage and cracking over a range of impact velocities is remarkable.

Fig. 13a additional shows measured and computed normalized rod lengths as a function of time for all three velocities under consideration, by way of quantitative validation. By this metric, the results of the simulations match the observed trends and are in fair agreement with the experimental measurements. It bears emphasis that the model employed in the simulations is remarkable for its simplicity, both as regards the bulk behavior of the material and its fracture properties, and that no effort has been made to enhance the model in order to improve the fit to experiments. Given the simplicity of the model, the quantitative agreement shown in Fig. 13a may be regarded as

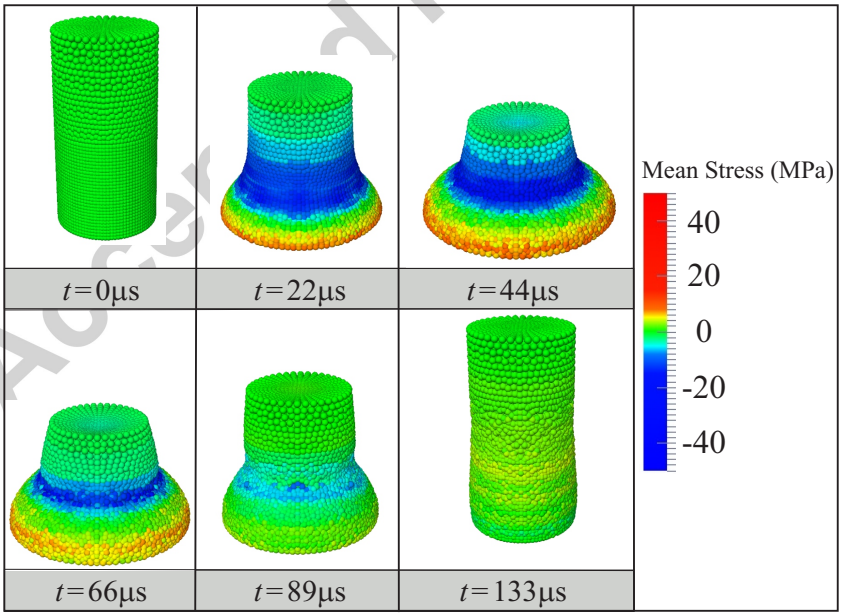

Figure 7: Snapshots of simulation at $v = 245$ m/s impact velocity.

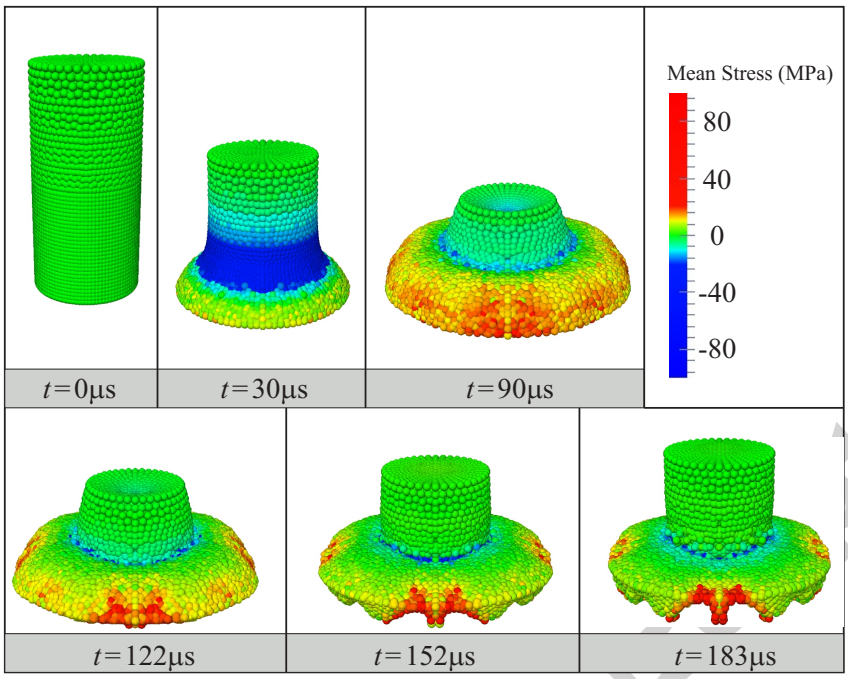

Figure 8: Snapshots of simulation at $v = 332$ m/s impact velocity.

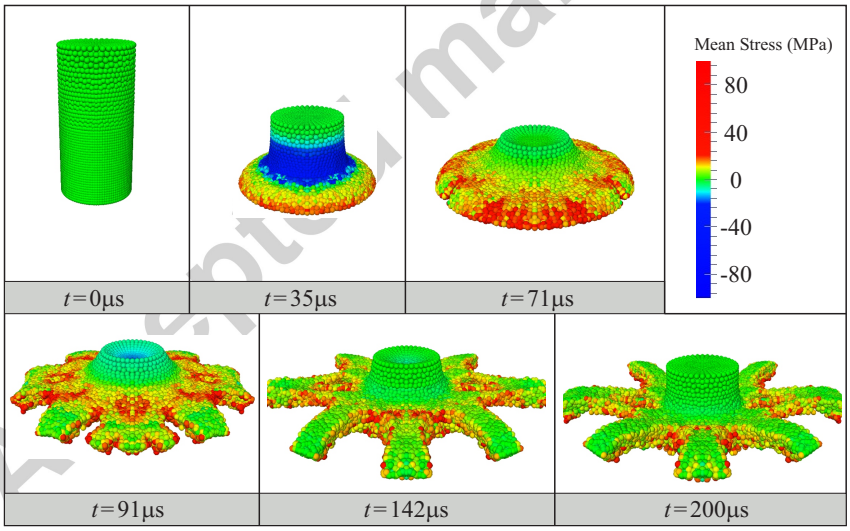

Figure 9: Snapshots of simulation at $v = 424$ m/s impact velocity.

furnishing a modicum of validation of the overall framework. For completeness, Fig. 13b additionally shows the variation of the computed specimen length with mesh size by way of convergence analysis. A clear trend towards convergence, with superlinear convergence rate $\alpha = 1.27$ is evinced by the

Figure 10: Patterns of damage in recovered specimen after shot at impact speed $v = 245m/s$. Left: Experiment. Right: Simulation.

figure.

6. Summary and concluding remarks

We have developed a simple one-parameter macroscopic model of distributed damage and fracture of polymers. We begin by assuming that the material behavior has two components, local and nonlocal. The local component characterizes the behavior of large material samples deforming uniformly and it represents the configurational statistics of a polymeric chain network in the thermodynamic limit. In order to account for damage, we extend the classical network theory by assuming that the chain bonds have a finite strength. We show that, for large deformations, the corresponding deformation-theoretical free energy has zero growth, i. e., it is bounded above and below by a constant. We assume that, in polymers undergoing fracture, this inherently unstable behavior is held in check by a second fundamental property, namely, the fractional strain-gradient elasticity. We further assume that the non-local component of the material behavior is characterized by fractional strain-gradient elasticity with linear growth in the strain gradient. This latter growth assumption allows for deformation jumps across sharp interfaces. Under these conditions, we show that fracture

Figure 11: Patterns of damage in recovered specimen after shot at impact speed $v = 332m/s$. Left: Experiment. Right: Simulation.

emerges as the net result of two competing effects: localization of deformation to failure planes promoted by the zero-growth of the local energy and the stabilizing effect of fractional strain-gradient elasticity. We specifically derive optimal scaling laws for the macroscopic fracture energy in the form of matching upper and lower bounds. The macroscopic fracture model that results from the optimal scaling analysis is characterized by a single parameter, namely, the critical energy-release rate. Conveniently, such a model is amenable to a straightforward numerical implementation by recourse to material-point eigenerosion, an averaged material-point erosion scheme that is known to converge in the limit of zero mesh size. We have demonstrated the range and fidelity of the damage and fracture criterion formulated in the foregoing by means of an example of application: The Taylor-impact experiments of Mock and Drotar (2006) on polyurea 1000 specimens. Remarkably, despite its simplicity the model captures qualitatively both the patterns of distributed damage and cracking or tearing over the experimental range of impact velocities. The simulations are also in fair agreement with quantitative metrics such as the specimen length and exhibit robust convergence with respect to mesh size.

The essential role of the intrinsic length ℓ in determining the optimal

Figure 12: Patterns of damage in recovered specimen after shot at impact speed $v = 424m/s$. Left: Experiment. Right: Simulation.

scaling behavior is particularly noteworthy. Thus, if $\ell = 0$, i. e., if the material is local, then we see from (37) that the energy is bounded above by a bound that is linear in a, the fibril spacing. Evidently, the least upper bound is then zero and is attained for $a = 0$, in agreement with (36), i. e., the energy relaxes to zero as a result of localization of deformations to a negligibly thin band. Thus, in the absence of an internal length scale the fracture energy degenerates to zero, as expected from the sublinear growth of the energy, and the solid can fracture spontaneously at no energy cost. This unstable and pathological behavior of the local energy is stabilized by the non-local energy. Indeed, the lower bound (38) shows that, with $\ell > 0$, fracture indeed requires a well-defined energy per unit area, or specific fracture energy. The antagonistic roles of sublinear energy growth, characteristic of polymers undergoing damage, and the fractional strain-gradient elasticity in shaping the effective fracture properties of the material are remarkable.

The experimental validation presented here suggests that a very simple model of bulk behavior and fracture suffices to characterize qualitatively, and to a fair quantitative degree, complex aspects of the dynamic behavior and failure of polymers, including large deformations, patterns of distributed damage and fracture patterns. We remark that the preponderance

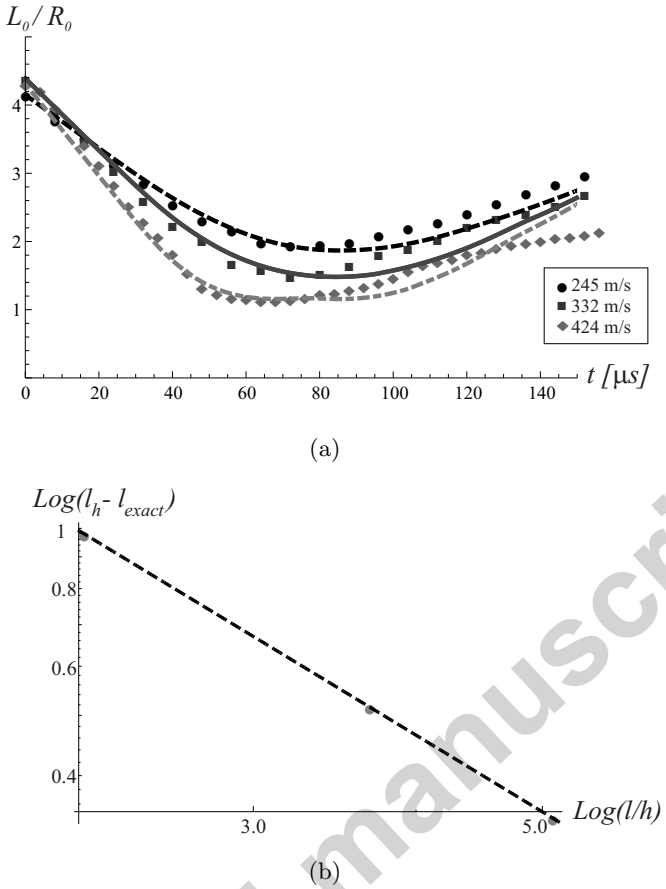

Figure 13: a) Normalized specimen height versus time at impact speeds $v = 245$ m/s (dashed), $v = 332$ m/s (solid) and $v = 424$ m/s (dash-dotted). b) Logarithmic convergence plot showing total accumulated specimen length over time for different mesh sizes.

of fracture mechanics pertains to materials that undergo small overall deformations, be them elastic or plastic. Thus, the ability of the model to characterize fracture in solids undergoing exceedingly large deformations, including the retraction of cracks upon unloading, is remarkable. The ability of tensile tests to supply estimates of the critical energy-release rate, also in the context of very large deformations, is also noteworthy. We conclude by noting that, while its qualitative predictiveness and micromechanical foundations lend strong support to the overall modeling framework, further modeling enhancements may be desirable with a view to improving its quantitative fidelity.

Acknowledgements

SH and MO gratefully acknowledge support from the Office of Naval Research through grant N00014-11-1-0547. SH and MO also gratefully acknowledge the support of the U.S. National Science Foundation through the Partnership for International Research and Education (PIRE) on Science at the Triple Point Between Mathematics, Mechanics and Materials Science, Award Number 0967140. SH gratefully acknowledges support provided by the Institute for Applied Mathematics (IAM), University of Bonn, Germany.

Appendix A. Upper-bound crazing construction

For completeness, we proceed to summarize the calculation of the upper bound. A detailed account of the calculation, as well as the derivation of the corresponding lower bound, may be found in Conti and Ortiz (2014).

We begin by defining a deformation mapping which describes, in a simple manner, the process of crazing in the layer $(0, L)^2 \times (-a, a) \subset \Omega$. Elsewhere, the test deformation mapping is chosen as a rigid translation, namely,

$$\boldsymbol{y} = \boldsymbol{x} + \delta \boldsymbol{e}_3, \quad \text{for } x_3 \geq a, \text{ and } \boldsymbol{y} = \boldsymbol{x} - \delta \boldsymbol{e}_3, \quad \text{for } x_3 \leq -a, \tag{A.1}$$

where $\boldsymbol{e}_3$ is the transverse unit vector. The local term can be immediately estimated to give A_0 on the entire volume plus a quantity bounded by k_U on the central region, totaling $2L^2 A_0 H + 2k_U L^2 a$. This gives the first two terms in (36). We remark that, since the energy has zero growth, the details of the mapping are not needed to estimate the local part of the energy.

In order to estimate the nonlocal term we need to construct the mapping in $(0, L)^2 \times (-a, a)$ in detail. First the layer is subdivided into $\sim L^2/a^2$ cubes of side length $2a$. We may then focus on a single cube $C = (-a, a)^3$, the others being identical up to translations. We additionally confine attention to the prism $P = \{x_1 \geq 0,\ -x_1 \leq x_2 \leq x_1, -a \leq x_3 \leq a\}$, and extend the deformation mapping to the remainder of the cube by symmetry. We specifically aim to construct a volume-preserving mapping that opens a cavity around the segment $x_1 = a$, $x_3 = 0$, through the composition of three elementary mappings. We proceed to define each of these mappings in turn.

We begin by defining a constant-determinant mapping $\boldsymbol{f}$ that collapses the half-cube $H = C \cap \{x_1 \geq 0\}$ into P, Fig. A.14. To this end, we consider the class of mappings

$$f_1(\boldsymbol{x}) = h(x_1), \qquad f_2(\boldsymbol{x}) = \frac{x_2}{a} h(x_1), \qquad f_3(\boldsymbol{x}) = x_3, \tag{A.2}$$

subject to the ancillary conditions $h(0) = 0$ and $h(a) = a$. This class of mappings transforms planes $x_1 =$ constant to planes $y_1 =$ constant. We have

$$\det(\nabla \boldsymbol{f}) = \frac{h h'}{a} = C, \tag{A.3}$$

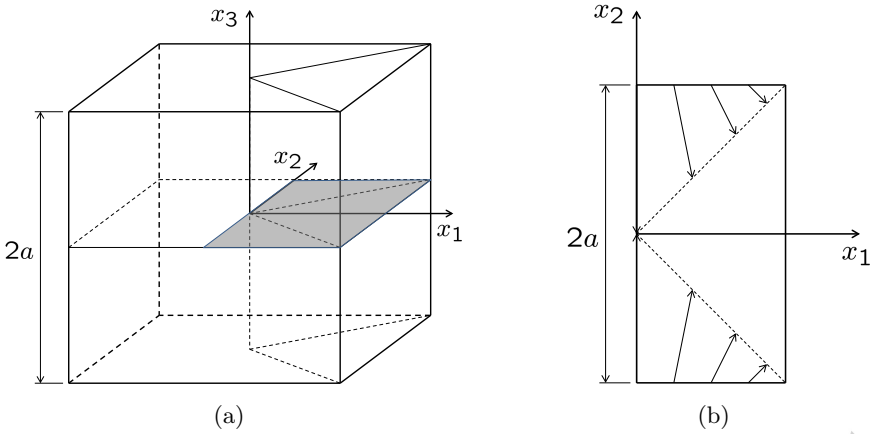

Figure A.14: Schematic of first mapping $\boldsymbol{f}$ used in the upper bound construction.

where C is a constant. Integrating once gives

$$h = \sqrt{2Cax_1}, \tag{A.4}$$

where we have used the condition $h(0) = 0$. From the second condition $h(a) = a$ we obtain

$$\det(\nabla \boldsymbol{f}) = C = \frac{1}{2}, \tag{A.5}$$

and

$$f_1(\boldsymbol{x}) = \sqrt{ax_1}, \qquad f_2(\boldsymbol{x}) = x_2\sqrt{\frac{x_1}{a}}, \qquad f_3(\boldsymbol{x}) = x_3. \tag{A.6}$$

This mapping is readily inverted to give

$$f_1^{-1}(\boldsymbol{y}) = \frac{y_1^2}{a}, \qquad f_2^{-1}(\boldsymbol{y}) = a\frac{y_2}{y_1}, \qquad f_3^{-1}(\boldsymbol{y}) = y_3. \tag{A.7}$$

Next we construct a second constant-determinant mapping that opens up a prismatic cavity around the segment $x_1 = a$, $x_3 = 0$. To this end, we restrict attention to the subdomain $0 \le x_3 \le a - x_1$ and subsequently extend the resulting mapping to the to the region $x_3 \ge a - x_1$ by exchanging x_3 and $a - x_1$. Finally, the mapping is extended to the entire half-plane $x_1 \ge 0$ by reflection about the plane $x_3 = 0$. We specifically consider the class of mappings

$$g_1(\boldsymbol{x}) = k(x_1), \qquad g_2(\boldsymbol{x}) = x_2, \qquad g_3(\boldsymbol{x}) = \frac{a - k(x_1)}{a - x_1}x_3, \tag{A.8}$$

subject to the ancillary condition $k(0) = 0$. This class of mappings transforms planes $x_1 =$ constant to planes $y_1 =$ constant. We have

$$\det(\nabla \boldsymbol{g}) = \frac{a - k}{a - x_1}k' = \frac{1}{\lambda}, \tag{A.9}$$

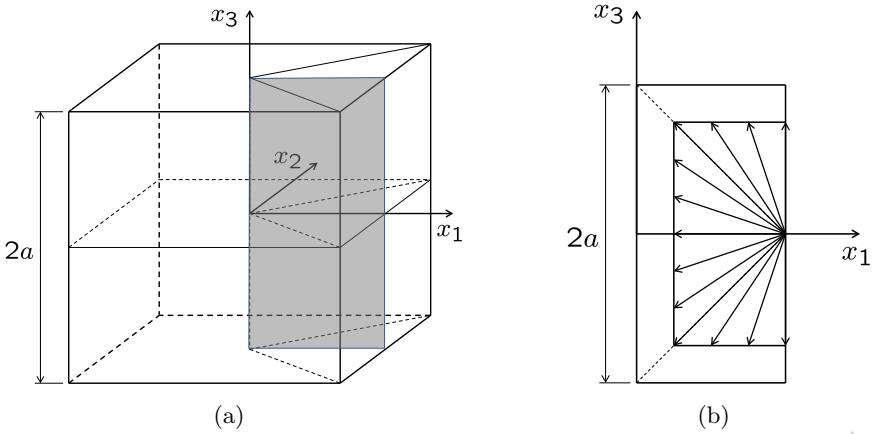

Figure A.15: Schematic of second mapping $\boldsymbol{g}$ used in the upper bound construction.

where $\lambda \geq 1$ is a constant. Integrating once gives

$$ak - \frac{k^2}{2} = \frac{1}{\lambda}\left(ax_1 - \frac{x_1^2}{2}\right), \tag{A.10}$$

where we have used the condition $k(0) = 0$. Solving for k we obtain, explicitly,

$$k(x_1) = a - \sqrt{a^2 - \frac{2}{\lambda}\left(ax_1 - \frac{x_1^2}{2}\right)}. \tag{A.11}$$

For $a - x_1 \leq x_3 \leq a$ we instead use

$$g_1(\boldsymbol{x}) = a - \frac{a - k(a - x_3)}{x_3}(a - x_1), \quad g_2(\boldsymbol{x}) = x_2, \quad g_3(\boldsymbol{x}) = a - k(a - x_3) \tag{A.12}$$

with the same function k.

We finally define a volume-preserving deformation mapping that describes the formation of a fibril around the x_3-axis and that reduces to the identity on the planes $x_3 = \pm a$ through the composition of mappings

$$y_1 = f_1(\boldsymbol{g}(\boldsymbol{f}^{-1}(\boldsymbol{x}))), \quad y_2 = f_2(\boldsymbol{g}(\boldsymbol{f}^{-1}(\boldsymbol{x}))), \quad y_3 = \lambda f_3(\boldsymbol{g}(\boldsymbol{f}^{-1}(\boldsymbol{x}))), \tag{A.13}$$

where the factor of λ represents a uniform extension in the x_3 direction. This operation completes the definition of the test deformation mapping. A direct computation gives, explicitly,

$$\begin{aligned} y_1 &= \sqrt{a^2 - \sqrt{a^4 - \lambda^{-1}(2a^2x_1^2 - x_1^4)}}, \\ y_2 &= \frac{y_1 x_2}{x_1}, \qquad y_3 = \frac{\lambda(a^2 - y_1^2)x_3}{a^2 - x_1^2}, \end{aligned} \tag{A.14}$$

over the domain $P \cap \{a|x_3| + x_1^2 \le a^2\}$, and

$$\begin{aligned} y_1 &= \sqrt{a^2 - \frac{a^2 - x_1^2}{x_3}\sqrt{1 - \lambda^{-1}(a^2 - x_3^2)}}, \\ y_2 &= \frac{y_1 x_2}{x_1}, \qquad y_3 = \lambda \operatorname{sgn}(x_3) \sqrt{a^2 - \lambda^{-1}(a^2 - x_3^2)}, \end{aligned} \tag{A.15}$$

over the domain $P \cap \{ax_3 + x_1^2 \ge a^2\}$.

It is readily verified that $\det Dy = 1$ everywhere, that the deformation mapping $\boldsymbol{y}$ obeys the boundary data (A.1), that the two expressions match continuously on $|x_3| + x_1^2 = a$ and that $\boldsymbol{y}$ maps the planes $x_1 = \pm x_2$ and the plane $x_1 = a$ into themselves and can therefore be extended to the rest of the slab by symmetry.

It only remains to estimate the fractional norm. For the homogeneous $W^{\sigma,1}(\Omega)$ seminorm of a function $\boldsymbol{u} : \mathbb{R}^3 \to \mathbb{R}^m$, we use the definition based on traces, namely,

$$|\boldsymbol{u}|_{W^{\sigma,1}(\Omega)} = \inf \left\{ \int_0^\infty \int_{\mathbb{R}^3} \frac{|\partial_t \boldsymbol{f}| + |D\boldsymbol{f}|}{t^\sigma} dt : \boldsymbol{f}(0,\cdot) = \boldsymbol{u} \right\}, \tag{A.16}$$

see for example Adams (1975); Tartar (2007); Lunardi (2009). Here $\boldsymbol{f} : [0,\infty) \times \mathbb{R}^3 \to \mathbb{R}^m$ is an extension of $\boldsymbol{u}$, $D\boldsymbol{f}$ represents its distributional spatial derivative, and $\partial_t \boldsymbol{f}$ its distributional derivative in the new variable t.

We begin by considering the set $P_a = P \cap \{a|x_3| + x_1^2 \le a^2\}$, where $\boldsymbol{y}$ is defined by (A.14). A straightforward computation shows that, in this set,

$$|D\boldsymbol{y}|(\boldsymbol{x}) \le \frac{ca\lambda}{a - x_1}\,. \tag{A.17}$$

Set

$$\boldsymbol{f}(\boldsymbol{x}, t) = D\boldsymbol{y}(\boldsymbol{x}) \chi_{[0, a-x_1]}(t) \chi_{P_a}(\boldsymbol{x}), \tag{A.18}$$

where χ_E is the characteristic function of set E. From (A.16) we obtain, after lengthy computations,

$$|D\boldsymbol{y}\chi_{P_a}|_{W^{\sigma,1}(\Omega)} \le \int_0^\infty \int_{\mathbb{R}^3} \frac{|\partial_t \boldsymbol{f}| + |D\boldsymbol{f}|}{t^\sigma}\, dx\, dt \le c\lambda a^{3-\sigma}\,. \tag{A.19}$$

In computing the integral of $|D\boldsymbol{f}|$ we use that $D\boldsymbol{y}$ can be written as a sum of finitely many terms, each of which is monotone in each variable and obeys a bound of the type (A.17). Each volume integral is then evaluated using Gauss' theorem (cf. also Fokoua et al. (2013, 2014)).

We now turn attention to the set $P_b = P \cap \{ax_3 + x_1^2 \ge a^2\}$. The estimate (A.17) is now replaced by

$$|D\boldsymbol{y}|(\boldsymbol{x}) \le \frac{c\,a^2}{x_3 y_1(\boldsymbol{x})}\,, \tag{A.20}$$

complemented by

$$y_1(\boldsymbol{x}) \geq \min\left\{\sqrt{\frac{ax_3 + x_1^2 - a^2}{x_3/a}}, \sqrt{\frac{a^2 - x_3^2}{2\lambda}}\right\}. \tag{A.21}$$

We det

$$\boldsymbol{f}(\boldsymbol{x}, t) = D\boldsymbol{y}(\boldsymbol{x})\chi_{[0,T(\boldsymbol{x})]}(t)\chi_{P_a}(\boldsymbol{x}), \quad T(\boldsymbol{x}) = \sqrt{x_3(x_3 + x_1^2/a - a)}. \tag{A.22}$$

Another lengthy calculation leads to an estimate similar to (A.19). Summing over the L^2/a^2 cubes we conclude that

$$|D\boldsymbol{y}|_{W^{\sigma,1}(\Omega)} \leq cL^2\lambda\, a^{1-\sigma}. \tag{A.23}$$

Recalling that $\lambda = 1 + \delta/a$, we finally obtain the second term in (36).

Bibliography

Adams, R. A., 1975. Sobolev Spaces. Academic Press, New York-London, pure and Applied Mathematics, Vol. 65.

Agar, A. W., Frank, F. C., Keller, A., 1959. Crystallinity effects in the electron microscopy of polyethylene. Philosophical Magazine 4 (37), 32–55.

Alcazar, D., Ruan, J. R., Thierry, A., Kawaguchi, A., Lotz, B., 2006. Polysynthetic twinning in poly (vinylcyclohexane) single crystals and "fractional" secondary nucleation in polymer crystal growth. Macromolecules 39 (3), 1008–1019.

Alger, M. S. M., 1997. Polymer Science Dictionary. Springer.

Andrews, E. H., 1968. Fracture in Polymers. American Elsevier, New York.

Argon, A. S., 2013. The Physics of Deformation and Fracture of Polymers. Cambridge University Press, Cambridge.

Arroyo, M., Ortiz, M., 2006. Local maximum-entropy approximation schemes: a seamless bridge between finite elements and meshfree methods. International Journal for Numerical Methods in Engineering 65 (13), 2167–2202.

Baljon, A. R. C., Robbins, M. O., 2001. Simulations of crazing in polymer glasses: Effect of chain length and surface tension. Macromolecules 34 (12), 4200–4209.

Ball, J. M., 1982. Discontinuous equilibrium solutions and cavitation in nonlinear elasticity. Philos. Trans. Roy. Soc. London Ser. A 306 (1496), 557–611.

Basu, S., Mahajan, D. K., Van der Giessen, E., 2005. Micromechanics of the growth of a craze fibril in glassy polymers. Polymer 46 (18), 7504–7518.

Bikales, N. M., 1971. Mechanical Properties of Polymers. Encyclopedia reprints. Wiley-Interscience, New York.

Cho, K., Gent, A. N., 1988. Cavitation in model elastomeric composites. Journal of Materials Science 23 (1), 141–144.

Choksi, R., Kohn, R. V., Otto, F., 1999. Domain branching in uniaxial ferromagnets: a scaling law for the minimum energy. Comm. Math. Phys. 201, 61–79.

Conti, S., 2000. Branched microstructures: scaling and asymptotic self-similarity. Comm. Pure Appl. Math. 53, 1448–1474.

Conti, S., DeLellis, C., 2003. Some remarks on the theory of elasticity for compressible neohookean materials. Ann. Scuola Norm. Sup. Pisa Cl. Sci. (5), 521–549.

Conti, S., Ortiz, M., 2005. Dislocation microstructures and the effective behavior of single crystals. Arch. Rat. Mech. Anal. 176, 103–147.

Conti, S., Ortiz, M., 2014. Optimal scaling in solids undergoing ductile fracture by crazing, (in preparation).

Donald, A. M., Kramer, E. J., 1982. The competition between shear deformation and crazing in glassy-polymers. Journal of Materials Science 17 (7), 1871–1879.

Drozdov, A. D., 2001. Modelling nonlinear viscoelasticity and damage in amorphous glassy polymers. Mathematical and Computer Modelling 33 (8-9), 883–893.

El Sayed, T., Mock, W., Mota, A., Fraternali, F., Ortiz, M., 2009. Computational assessment of ballistic impact on a high strength structural steel/polyurea composite plate. Computational Mechanics 43 (4), 525–534.

Estevez, R., Basu, S., Van Der Giessen, E., 2000a. A thermo-mechanical investigation of the influence of shear yielding and crazing on fracture characteristics of glassy polymers. Advances in Mechanical Behaviour, Plasticity and Damage, Vols 1 and 2, Proceedings, 225–230.

Estevez, R., Tijssens, M. G. A., Van der Giessen, E., 2000b. Modeling of the competition between shear yielding and crazing in glassy polymers. Journal of the Mechanics and Physics of Solids 48 (12), 2585–2617.

Fleck, N. A., Hutchinson, J. W., 1993. A phenomenological theory for strain gradient effects in plasticity. Journal of the Mechanics and Physics of Solids 41 (12), 1825–1857.

Fleck, N. A., Hutchinson, J. W., 1997. Strain gradient plasticity. Advances in Applied Mechanics 33, 295–361.

Fleck, N. A., Hutchinson, J. W., 2001. A reformulation of strain gradient plasticity. Journal of the Mechanics and Physics of Solids 49 (10), 2245–2271.

Fleck, N. A., Muller, G. M., Ashby, M. F., Hutchinson, J. W., 1994. Strain gradient plasticity - theory and experiment. Acta Metallurgica Et Materialia 42 (2), 475–487.

Flory, P. J., 1989. Statistical Mechanics of Chain Molecules. Hanser Publishers, Munich.

Fokoua, L., Conti, S., Ortiz, M., 2013. Optimal scaling in solids undergoing ductile fracture by void sheet formation, *Archive for Rational Mechanics and Analysis* (accepted for publication).

Fokoua, L., Conti, S., Ortiz, M., 2014. Optimal scaling laws for ductile fracture derived from strain-gradient microplasticity. J. Mech. Phys. Solids 62, 295–311.

Fortunelli, A., Geloni, C., Lazzeri, A., 2004. Simulation of the plastic behavior of amorphous glassy bis-phenol-a-polycarbonate. Journal of Chemical Physics 121 (10), 4941–4950.

Fortunelli, A., Ortiz, M., 2007. Constitutive model for plasticity in an amorphous polycarbonate. Physical Review E 76 (4).

Geil, P. H., 1963. Polymer Single Crystals. Polymer reviews,. Interscience Publishers, New York,.

Gent, A. N., 1973. Cavitation, crazing and fracture in glassy polymers. Bulletin of the American Physical Society 18 (3), 400–400.

Gent, A. N., Wang, C., 1991. Fracture-mechanics and cavitation in rubber-like solids. Journal of Materials Science 26 (12), 3392–3395.

Grellmann, W., Seidler, S., 2001. Deformation and Fracture Behavior of Polymers. Engineering materials. Springer, Berlin.

Henao, D., Mora-Corral, C., 2010. Invertibility and weak continuity of the determinant for the modelling of cavitation and fracture in nonlinear elasticity. Archive for Rational Mechanics and Analysis 197, 619–655.

Henkee, C. S., Kramer, E. J., 1986. Loss of entanglement density during crazing. Journal of Materials Science 21 (4), 1398–1404.

Hermann, G., 1974. R. D. Mindlin and Applied Mechanics; a collection of studies in the development of applied mechanics, dedicated to Professor Raymond D. Mindlin by his former students. Pergamon Press, New York,.

Huang, Y., Xue, Z., Gao, H., Nix, W. D., Xia, Z. C., 2000. A study of microindentation hardness tests by mechanism-based strain gradient plasticity. Journal of Materials Research 15 (8), 1786–1796.

Hutchinson, J. W., 1968. Singular behaviour at end of a tensile crack in a hardening material. Journal of the Mechanics and Physics of Solids 16 (1), 13–31.

Hutchison, J. W., 1979. A course on nonlinear fracture mechanics. Dept. Solid Mechanics, TU Denmark.

James, R. D., Spector, S. J., 1991. The formation of filamentary voids in solids. J. Mech. Phys. Solids 39 (6), 783–813.

Jiao, T., Clifton, R. J., Grunschel, S. E., 2006. High strain rate response of an elastomer. Shock Compression of Condensed Matter - 2005, Pts 1 and 2 845, 809–812.

Jiao, T., Clifton, R. J., Grunschel, S. E., 2007. Pressure-sensitivity and tensile strength of an elastomer at high strain rates. Shock Compression of Condensed Matter - 2007, Pts 1 and 2 955, 707–710.

Jiao, T., Clifton, R. J., Grunschel, S. E., 2009. Pressure-sensitivity and consititutive modeling of an elastomer at high strain rates. Shock Compression of Condensed Matter - 2009, Pts 1 and 2 1195, 1229–1232.

Kanninen, M. F., Popelar, C. H., 1985. Advanced Fracture Mechanics. Oxford engineering science series. Oxford University Press, New York.

Kausch, H. H. (Ed.), 1983. Crazing in Polymers. Springer-Verlag, Berlin.

Kausch, H. H., 1985. Polymer Fracture, 2nd Edition. Polymers, Properties and Applications. Springer-Verlag, Berlin.

Keller, A., 1968. Polymer crystals. Reports on Progress in Physics 31, 623.

Kiho, H., Geil, P. H., Peterlin, A., 1964. Polymer deformation (6) - twinning and phase transformation of polyethylene single crystals as function of stretching direction. Journal of Applied Physics 35 (5).

Kinloch, A. J., Young, R. J., 1983. Fracture Behaviour of Polymers. Applied Science Publishers, London.

Knauss, W. G., Zhao, J., 2007. Improved relaxation time coverage in ramp-strain histories. Mechanics of Time-Dependent Materials 11, 199–216.

Kohn, R. V., Müller, S., 1992. Branching of twins near an austenite-twinned-martensite interface. Phil. Mag. A 66, 697–715.

Kohn, R. V., Müller, S., 1994. Surface energy and microstructure in coherent phase transitions. Comm. Pure Appl. Math. 47, 405–435.

Kovacs, A. J., Lotz, B., Keller, A., 1969. Multiple twinning in polyethylene oxide singlecrystals - a scheme for formation of growth twins from self-seeding nuclei. Journal of Macromolecular Science-Physics B3 (3), 385.

Kramer, E. J., Berger, L. L., 1990. Fundamental processes of craze growth and fracture. Advances in Polymer Science 91/92, 1–68.

Kröner, E. (Ed.), 1968. Mechanics of Generalized Continua; proceedings of the IUTAM-symposium on the Generalized Cosserat Continuum and the Continuum Theory of Dislocations with Applications. Springer-Verlag, Freudenstadt and Stuttgart (Germany) 1967.

Krupenkin, T. N., Fredrickson, G. H., 1999a. Crazing in two and three dimensions. 1. two-dimensional crazing. Macromolecules 32 (15), 5029–5035.

Krupenkin, T. N., Fredrickson, G. H., 1999b. Crazing in two and three dimensions. 2. three-dimensional crazing. Macromolecules 32 (15), 5036–5045.

Leonov, A. I., Brown, H. R., 1991. A model of fibril deformation in crazes. Journal of Polymer Science. Part B - Polymer Physics 29 (2), 197–209.

Li, B., Habbal, F., Ortiz, M., 2010. Optimal transportation meshfree approximation schemes for fluid and plastic flows. International Journal for Numerical Methods in Engineering 83 (12), 1541–1579.

Li, B., Kidane, A., Ravichandran, G., Ortiz, M., 2012. Verification and validation of the Optimal Transportation Meshfree (OTM) simulation of terminal ballistics. International Journal of Impact Engineering 42, 25–36.

Lunardi, A., 2009. Interpolation theory, 2nd Edition. Appunti. Scuola Normale Superiore di Pisa (Nuova Serie). Edizioni della Normale, Pisa.

Martin, J. B., 1975. Plasticity : fundamentals and general results. MIT Press, Cambridge, Mass.

Maugin, G. A., Metrikine, A. V., 2010. Mechanics of Generalized Continua : one hundred years after the Cosserats. Advances in mechanics and mathematics,. Springer, New York.

McClintock, F. A., Argon, A. S., 1966. Mechanical Behavior of Materials. Addison-Wesley series in metallurgy and materials,. Addison-Wesley Pub. Co., Reading, Mass.

Mock, Jr. (presenter), W., Drotar, J., 2006. Penetration protection experiments using polymer materials. ONR Workshop, St. Michael's, Maryland.

Müller, S., Spector, S. J., 1995. An existence theory for nonlinear elasticity that allows for cavitation. Arch. Rat. Mech. Anal. 131, 1–66.

Nix, W. D., Gao, H. J., 1998. Indentation size effects in crystalline materials: A law for strain gradient plasticity. Journal of the Mechanics and Physics of Solids 46 (3), 411–425.

Ortiz, M., Stainier, L., 1999. The variational formulation of viscoplastic constitutive updates. Computer Methods in Applied Mechanics and Engineering 171 (3-4), 419–444.

Pandolfi, A., Ortiz, M., 2012. An eigenerosion approach to brittle fracture. International Journal for Numerical Methods in Engineering 92 (8), 694–714.

Pradère, P., Revol, J. F., Manley, R. S., 1988. Microdomains in poly(4-methylpentene-1) single-crystals. Macromolecules 21 (9), 2747–2751.

Reina, C., Li, B., Weinberg, K., Ortiz, M., 2013. A micromechanical model of distributed damage due to void growth in general materials and under general deformation histories. International Journal for Numerical Methods in Engineering 93 (6), 575–611.

Reneker, D. H., Geil, P. H., 1960. Morphology of polymer single crystals. Journal of Applied Physics 31 (11), 1916–1925.

Reppel, T., Dally, T., Weinberg, K., 2012. On the elastic modeling of highly extensible polyurea. Technische Mechanik 33 (1), 19–33.

Rice, J. R., 1968. A path independent integral and approximate analysis of strain concentration by notches and cracks. Journal of Applied Mechanics 35 (2), 379–386.

Rice, J. R., Rosengren, G. F., 1968. Plane strain deformation near a crack tip in a power-law hardening material. Journal of the Mechanics and Physics of Solids 16 (1), 1–12.

Rivlin, R. S., Thomas, A. G., 1953. Rupture of rubber. i. characteristic energy for tearing. Journal of Polymer Science 10, 291–318.

Rottler, J., Robbins, M. O., 2003. Growth, microstructure, and failure of crazes in glassy polymers. Physical Review E 68 (1).

Rottler, J., Robbins, M. O., 2004. Craze formation and the fracture energy of glassy polymers. Chaos 14 (4), 5–5.

Saad-Gouider, N., Estevez, R., Agnon, C., Seguela, R., 2006. Calibration of a viscoplastic cohesive zone for crazing in PMMA. Engineering Fracture Mechanics 73 (16), 2503–2522.

Sanderson, R. D., Pasch, H. (Eds.), 2004. Crazing and Fracture in Polymers: Micromechanisms and effect of molecular variables. Vol. 214.

Schmidt, B., Fraternali, F., Ortiz, M., 2009. Eigenfracture: An eigendeformation approach to variational fracture. Multiscale Modeling & Simulation 7 (3), 1237–1266.

Seelig, T., Van der Giessen, E., 2009. A cell model study of crazing and matrix plasticity in rubber-toughened glassy polymers. Computational Materials Science 45 (3), 725–728.

Socrate, S., Boyce, M. C., Lazzeri, A., 2001. A micromechanical model for multiple crazing in high impact polystyrene. Mechanics of Materials 33 (3), 155–175.

Tartar, L., 2007. An Introduction to Sobolev Spaces and Interpolation Spaces. Springer.

Tijssens, M. G. A., van der Giessen, E., 2002. A possible mechanism for cross-tie fibril generation in crazing of amorphous polymers. Polymer 43 (3), 831–838.

Tijssens, M. G. A., van der Giessen, E., Sluys, L. J., 2000a. Modeling of crazing using a cohesive surface methodology. Mechanics of Materials 32 (1), 19–35.

Tijssens, M. G. A., van der Giessen, E., Sluys, L. J., 2000b. Simulation of mode i crack growth in polymers by crazing. International Journal of Solids and Structures 37 (48-50), 7307–7327.

Weinberg, K., Reppel, T., 2013. Elastic response and damage by cavitation in polyurea. subm. to Exp. Mechanics.

Weiner, J. H., 2002. Statistical Mechanics of Elasticity, 2nd Edition. Dover Publications, Mineola, N. Y.

Williams, J. G., 1984. Fracture Mechanics of Polymers. Ellis Horwood series in engineering science. E. Horwood, Halsted Press, Chichester.

Wittmann, J. C., Kovacs, A. J., 1970. Multiple twins in polyethylene monocrystals. Berichte Der Bunsen-Gesellschaft Für Physikalische Chemie 74 (8-9), 901.

Xue, Z., Huang, Y., Gao, F., Nix, W. D., 2000. The strain gradient effects in micro-indentation hardness experiments. Multiscale Phenomena in Materials - Experiments and Modeling 578, 53–58.

Yong, Z., M., L. K., Ravi-Chandar, K., 2009. Direct extraction of rate-dependent tractionseparation laws for polyurea/steel interfaces. International Journal of Solids and Structures 46, 31–51.

Zairi, F., Nait-Abdelaziz, M., Gloaguen, J. M., Lefebvre, J. M., 2008. Modelling of the elasto-viscoplastic damage behaviour of glassy polymers. International Journal of Plasticity 24 (6), 945–965.

Zhao, J., Knauss, W., Ravichandran, G., 2007. Applicability of the timetemperature superposition principle in modeling dynamic response of a polyurea. Mechanics of Time-Dependent Materials 11, 289–308.